Nanoscale

Accepted Manuscript

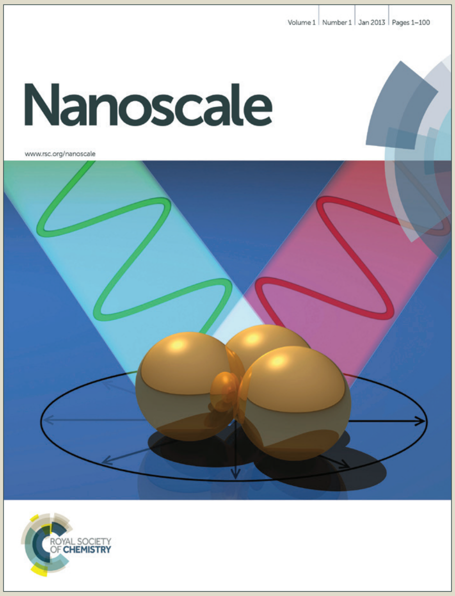

ROYAL SOCIETY OF CHEMISTRY

www.rsc.org/nanoscale

Nanoscale

Dynamic Article Links ►

Cite this: DOI: 10.1039/c0xx00000x

www.rsc.org/xxxxxx

ARTICLE TYPE

Three-Dimensional Hotspots in Evaporating Nanoparticle Sols for Ultrahigh Raman Scattering: Solid/Liquid Interface Effects†

Yudie Sun,[‡,a] Zhenzhen Han,[‡,a] Honglin Liu,[*,a] Shengnan He,[b] Liangbao Yang[*,a] and Jinhuai Liu[a]

Received (in XXX, XXX) Xth XXXXXXXXX 20XX, Accepted Xth XXXXXXXXX 20XX

DOI: 10.1039/b000000x

Three-dimensional (3D) hotspots for ultrahigh surface-enhanced Raman scattering (SERS) has been experimentally demonstrated by evaporating a droplet of citrate-Ag sols both on the hydrophobic and hydrophilic flat surfaces. Interestingly, the hydrophobic surface increased Raman enhancement by two orders of magnitude larger and exhibits a better signal stability than the hydrophilic one. This study highlights the differences of hydrophilic and hydrophobic surfaces in enhanced Raman scattering by the use of extremely diluted Rhodamine 6G as the SERS reporter. In situ synchrotron-radiation small-angle X-ray scattering (SR-SAXS) was employed to explore the evolution of the 3D geometry of Ag nanoparticles in a single droplet and verify the influence mechanism of this two kinds of surfaces. The ideal situation of 3D self-assembly of nanoparticles in the evaporation process is a collaborative behaviour, but our results evidenced that a progressive 3D self-assembly of nanoparticles was more preferred due to the interface effects. Our experimental data derived from in situ SR-SAXS reveals that a truly distinct 3D geometry of the Ag particles develops during the evaporation process on both hydrophilic and hydrophobic surfaces. In this type of 3D geometry, the increased uniformity of interparticle distance induced a sharp peak of SR-SAXS signals, differing significantly from the dry state. Particularly, the fluorosilylated surface reduces the interaction with particles and decreases the electrostatic adsorption on flat surface, which helps to control the interparticle distance to remain within a small range, produce a larger number of hot spots in 3D space, and amplify the SERS enhancement accordingly.

Introduction

The plasmonic hot-spot predominantly determines the capability of surface-enhanced Raman scattering (SERS).[1] Towards a practical analyzer, SERS technique faces three main challenges. The first one is the capability to produce a SERS-active substrate with large number of hot-spots that can give rise to high enhancement factors;[2] the second is the efficiency to place the targeted molecules in hot-spots;[3] and the third is the reproducibility of the first two issues. To date, many SERS-active structures have been developed, such as nanodumbbells[4], nanosphere,[5] chains[6], self-assembled clusters[7], arrays[8], however, most reported SERS hotspots have been shown to exist in zero-dimensional point-like, one-dimensional (1D) linear, or two-dimensional (2D) planar geometries that can potentially achieve high SERS enhancement factors, while the maximum number of SERS hot-spots that can be achieved for such substrates are limited to a single Cartesian plane. Since the laser confocal volume in SERS apparatus is a three-dimensional (3D) space, indicating that 1D and/or 2D arrays are under-utilizing the active confocal volume even though large-area hot-spots are precisely fabricated in planar geometry. Another limitation of 1D and 2D SERS substrates is that the incident laser should be tightly focused on the correct plane to achieve optimal Raman enhancement, which reduces the versatility of such substrates, especially for on-site applications.

To address these issues, 3D SERS-active substrates with considerable extension in the third dimension are actively pursued to increase the versatility of a 3D SERS platform, by increasing the number and utility of SERS hot-spots in all three dimensions.[9-11] The extension of a SERS substrate from 2D to 3D brings about a larger overall surface area which in turn enables more target molecules to be adsorbed and detected in the third dimension, especially along the z-axis.[12-14] Therefore, 3D architecture can achieve higher tolerance in focus misalignment along the z-direction.[15] To date, controlled assembly using colloidal chemistry is an emerging and promising field for high-yield production of 3D SERS-active clusters with small interparticle gaps. The SERS enhancement factor is highly related to the interparticle gap and the 3D coordination numbers of particles[16]. One point is certain that the extension of a SERS substrate from 2D to 3D can provide higher hot-spot densities per unit volume. However, it remains to be uncovered the most efficient 3D architecture as well as the optimal fabrication route, and an impartial comparison between structural variations in three dimensions on the SERS performance of a 3D SERS substrate has yet to be fully investigated.[14]

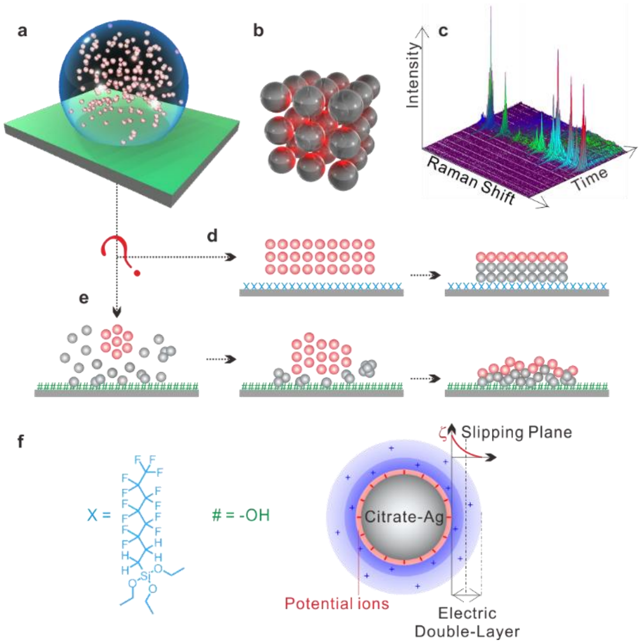

Scheme 1. Sketches representing (a) a droplet of Ag sols on a hydrophobic surface, (b) 3D hotspots geometry in the adhesive-force-constructed closely packed particles in 3D space formed in the water-evaporation process. c) Time-course SERS mapping of a 1-μl sample containing 50 pmol R6G ($\sim 3\times10^{13}$ molecules) and $\sim 10^{10}$ Ag particles placed on a fluorosilylated silicon wafer. Illustrated theological conjectures of 3D self-assembly: (d) collaborative or (e) progressive aggregating. (f) Illustrated structural formulas of fluorosilane and hydroxyl and the dielectric environment around a citrate-capped nanoparticle.

We recently demonstrated the existing of 3D hot-spot matrix that can hold hotspots between every two adjacent particles in 3D space, simply achieved by evaporating a droplet of citrate-Ag sols on a fluorosilylated silicon.[17] 3D hotspots owns excellent capability of detection sensitivity, besides the presence of liquid avoids the degradation of nanoparticles under laser irradiation[18-20]. When a droplet of citrate-Ag sols is dropped on silicon wafer, the interparticle gaps shrink gradually during the evaporating (Scheme 1a). During the evaporation process of a droplet of Ag sols, the van der Waals attraction and electrostatic repulsion mainly dominate particle-particle interactions which form ‘trapping well’ to immobilize particles in 3D space and create 3D SERS hotspot matrix (Scheme 1b and c), while this state only exists in a very short period of time because of interfacial effect, ion strength, particle density, thermal fluctuations, diffusion, or even humidity. In fact, robust control over the orientation and position of nanoparticles in 3D geometry remains a formidable challenge[21]. One of the urgent issues to be addressed is the solid/liquid interface effects on the formation of 3D hotspot matrix, i.e. how solid/liquid interface features affect the formation of 3D hotspot in space. In this contribution, we investigated the effects of hydrophilic and hydrophobic surfaces on SERS enhancement (Scheme 1e and d), and in situ synchrotron-radiation small-angle X-ray scattering (SR-SAXS) was employed to examine the deposition of nanoparticles and the formation of 3D hotspot matrix and the influence mechanism was figured out.

Experimental Section

Materials

$AgNO_3$ and citric acid were obtained from Shanghai Chemical Reagent Company (Shanghai, China). Rhodamine 6G (R6G) and triethoxy-1H,1H,2H,2H-tridecafluoro-n-octylsilane were obtained from Sigma Company (Shanghai, China). All reagents were of analytical grade and used as received without further purification. Ultrapure water (>18.0 MΩ cm) was purified using a Millipore Milli-Q (Suzhou, China) gradient system through-out experiment.

Instrument

The scanning electron microscopy (SEM) images were taken by using a field-emission scanning electron microscopy (FESEM, JEOL JSM-6700F, 10 kV). Contact angles of the droplets placed on different surfaces were measured using OCA-20 Data Physics Instruments GmbH. Raman spectra were collected on a LabRam HR800 confocal micro-Raman system (JY Horiba). The spectra were processed by the LabSpec V5.58.25 software, and the peak frequency and FWHM were obtained from peak fitting. In situ SR-SAXS measurements were performed at the μSpot beamline BL16B1 at SSRF (Shanghai, China). The beamline provide a divergence of 0.4 mrad (horizontally and vertically) and a beam diameter of ~200 μm with a maximal photon flux of 2×10^{13} photons/(s.10^{-3}BW) at 8.1 keV. The SAXS data were processed by the Fit2d and Irena software packages.[22]

Surface treatment of the silicon slice

Firstly, silicon slices were cleaned by immersing themselves in a boiling solution prepared by mixing 30% H_2O_2 and concentrated H_2SO_4 with a volume ratio of 1:3. After cooling, the substrates were rinsed repeatedly with ultrapure water. Then, The slices were immerged into 40 mM of triethoxy-1H,1H,2H,2H-tridecafluoro-n-octylsilane solution for 2 hours, rinsed with ethanol, dried under a stream of nitrogen.

Preparation of concentrated Ag sols

Ag nanoparticles with a diameter of approximately 60 nm was synthesized by the classic citric acid reduction method. 100 ml of the as-synthesized Ag sols was centrifuged at 10 000 rpm for 10 min. The concentration of as-prepared Ag sols was estimated to be approximately 10^{11} colloids/ml or, equivalently, ≈0.17 nM[17]. 1 ml of the Ag sols were centrifuged at 13,000 g for 3 min, and then 995 μl of the colorless supernatant was discarded. The remaining 5 μl of the black pellet was re-dispersed under sonication and used as the SERS substrate. The concentrated Ag sols is estimated to be approximately 10^{10} particle/μl. 5 μl of the analyte solution was added into 5 μl of the concentrated Ag sols, which was then mixed by ultrasonic dispersing method for 10 min. A longer time treatment was also tested, and no significant influence was found.

SERS Measurements

A droplet of 1 μl Ag sols mixed with the analytes was dropped on the silicon slide. The laser was first focused on the surface of silicon slide through the top of the droplet. Time-course SERS mapping was performed at room temperature with a humidity of 50% by the use of a 532-nm laser with 1 mW power and

50×objective (~1 μm^2 spot). The integral time is 1 s and aperture is 50 μm slit. The interval period for the collection of Raman spectra was set at 0.2 s.

Results and discussion

Interface effects on SERS performance of 3D hotspots

The SERS performance of 3D hotspots in an evaporating Ag sols on fluorosilylated silicon surface has been demonstrated in our previous work.[17] In this section, we mainly focused on the interface effects on the SERS performance. Time-course SERS mapping was performed to monitor the evaporation of a 1 μl sample on hydroxylated surface (Fig. 1a). This initial sample contained 0.5 nM rhodamine 6G (R6G). During the first 300 s, extremely weak Raman signals were observed which could be attributed to the Raman scattering of individual nanoparticles. Nevertheless, the fingerprints of R6G gradually enhanced after ~300 s; the fitted peak at about 1650 cm^{-1} has an intensity of about 1000 cnts (Fig. 1a), but its peak shape has large fluctuations (Figs. 1b-d). Gradually, these weak signals became stronger and reached the largest values at ~500 s. However, after ~600 s, the peak intensity rapidly decreased to below approximately 200 cps, and the peak shape again fluctuated drastically.

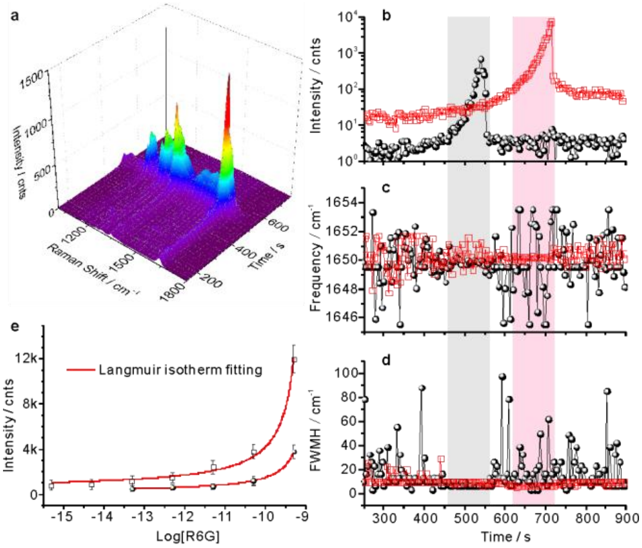

Figure 1. (a) Time-course SERS mapping of a 1 μL sample with 0.5 nM R6G and ~10^{10} Ag particles placed on a hydrophilic-treated silicon wafer. The corresponding time evolution of the (b) intensity, (c) frequency, and (d) full width at half-maximum (FWHM) of the 1650 cm^{-1} peak both on hydrophilic (solid circles) and hydrophobic (open squares) surface. (e) SERS intensity at 1650 cm^{-1} for different concentrations of R6G on hydrophilic (solid circles) and hydrophobic (open squares), respectively. The solid curve represents the Langmuir isotherm fit to the experimental data.

Figs. 1b-d plotted the changing of intensity, position and FWHM of the 1650 cm^{-1} peak during the time-course SERS mapping by the use of the hydroxylated and fluorosilylated silicon surface, respectively. The comparison indicated a same changing tendency, but the maximal peak intensity recorded on fluorosilylated surface was at least one order magnitude larger than that on hydroxylated surface. At the second stage when the signal enhanced quickly, both the peak frequency and FWHM became stable no matter on what type of interfacial. Nevertheless, the signals on hydrophobic surface was steadier than that on hydrophilic surface. In this regard, the hydrophobic surface provides the capability for improving the detection limit. To explore the detection limit on different interfacial, a series of low concentrations of R6G aqueous solutions ranging from1 0.5 nM to 0.5 fM were measured. The concentration of the as-prepared Ag sols is estimated to be approximately 10^{10} particle/μl.[23] The hydrophobic surface can improve the detection limit of R6G by two orders of magnitude (Fig. 1e). It is interesting to note that the SERS signal intensity changes little when the concentration lowered 5 pM (Fig. 1e). And the Langumir isotherm fitting (Red lines in Fig. 1e) implying a limited number of R6G molecules adsorbed to the hot-spot areas.[24] Moreover, the maximal intensity appeared at a much later moment (Fig. 1b), which is consistent with the result that the evaporation process on hydrophobic surface lasted a longer time than hydrophilic surface (Fig. 2), indicating that the organization of Ag particles at the late-stage of the evaporation process should be responsible for the great SERS enhancement.

To verify the effect of focal depth, we calculated the laser focal volume under our experimental conditions, and the calculated focal depth is ca. 9.6 μm and the laser spot size is ca. 1.3 μm (Fig. S1). In the initial droplet of Ag sols, the droplet height is about 740 μm (Fig. 2d), and the calculated average interparticle gap is larger than 400 nm. At this moment, even if the SERS signals appear, these signals should be originated from the single-particle's enhancement in liquid, and the focal depth can affect the signal intensities. When the droplet height decreased to ca. 10 μm, the averaged interparticle gap decreased to ca. 20~30 nm. In other words, the particle-particle coupling of the electric-field is not significant even if the droplet height decrease to the level of focal depth. Within the first 500 s of the evaporation process (Figs. 1a and 1b), the intensity of SERS signals only had a 5-fold enhancement. We consider that this enhancement should be mainly contributed from the concentration and enrichment of the particles and molecules, i.e. the focal depth mainly contributes to SERS intensity in this stage.

In the late-stage of the evaporation process, the droplet surface became nearly flat (Fig. 2d) and the deposition volume could be considered as a cylinder. Hence, the number of partciles within the scope of laser spot can be calculated by the following formula: Number of particle in laser spot = total number of particles $*\Phi^2/d^2$, where the spot size Φ is a constant and the d value nearly has no changes when the droplet height reduced to below 10 μm, which will be diccussed in detail in the next section. In other words, the number of particles in laser spot nearly has no changes in the late-stage of the evaporation process. We also carried out similar experiments with over-focus and under-focus (as illustrated in Fig. S1). The experimental results evidenced that similar exponential increase of the SERS signals was still existed, indicating that the focal depth was not responsible for the large SERS enhancement during the late-stage of the evaporation process. The SERS intensity falling off was not caused by the exact location of the laser focus. Hence, we concluded that only the presence of 3D hotspots in space can explain the exponential increase of the SERS signals, and the subsequent complete drying further destroys these liquid force constrtucted 3D gyomety of particles in space and quenchs the 3D hotspots. There are three factors contribute to this phenomenon when the intreparticle gap is smaller than 1 nm: First, the arising of quantum tunneling will dramatically reduce the electromagnetic enhancement ability; Second, charge-exchange effect will occur, leading to a decrease in the electric-field enhancement; and finally solid contacts among particles makes the entire aggregate behave as an equipotential body and thus give rise to an electrostatic shielding phenomenon.

Nanoparticle deposition

The drying of a colloidal droplet placed on a flat surface typically produces a ring-like stain. This phenomenon is commonly known as the coffee-ring effect and has been observed for a wide combination of suspended particles, surfaces, and solvents.[25] Earlier reports implied that the hydrophobic surface would weaken this phenomenon, and the more hydrophobic the harder to form coffee ring.[26] Nonetheless, the interface effect on SERS enhancement of 3D nanoparticle architecture remains unclear with regard to the evaporation properties of a colloidal droplet on both hydrophilic and hydrophobic surfaces. Here, the evaporation process of single droplet of Ag sols placed on different silicon slides was studied to investigate the deposition of suspensions containing nanoparticles over time, and the droplets placed on different surface were dried in air under temperature 25 ℃, humidity 50% without direct sunshine.

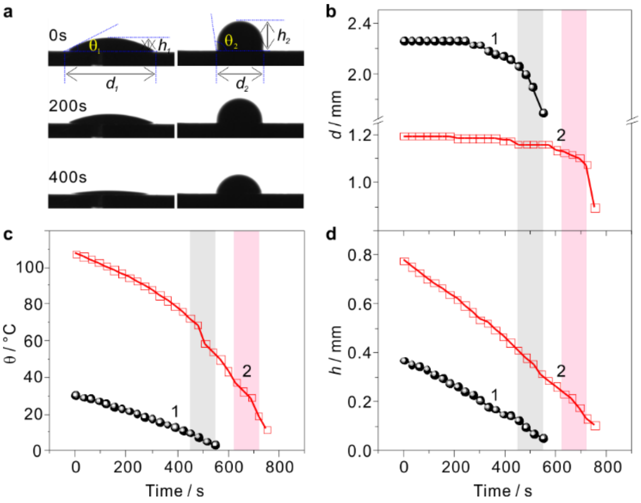

Figure 2. (a) Optical observations on the different stages of a single Ag sols droplet on hydrophilic (left) and hydrophobic (right) surfaces. And Time-course observation of the evaporation on the (b) deposition diameter, (c) contact angle, and (d) droplet height on hydrophilic (solid circles) and hydrophobic (open squares) surfaces, respectively. The initial volume of each droplet was 1 μl.

We drop 1 μl concentrated Ag sols on hydrophobic and hydrophilic surfaces, respectively. The droplet on hydrophobic silicon slides has a contact angle of 102 degrees, as shown in Fig. 2a. Then we use filter paper to remove the non-deposited nanoparticles in the drops every 3 minutes. Fig. S2 showed SEM observations on the particle adsorption on the fluorosilylated and the hydroxylated surfaces at different times during the evaporation of a single droplet of Ag sols. As a result, there are no particles deposited on the hydrophobic surface until all the solvent is exhausted (Fig. S2a). When the drop is dried, all nanoparticles deposited on the hydrophobic surface evenly. While a ring formed on the hydrophilic surface only 3 minutes after 1 μl sols was dropped (Fig. S2b). Then coffee ring structure was formed when all the moist water of the drops is exhausted by evaporation. These results further corroborated that the "coffee ring effect" was greatly weakened on hydrophobic surface and the liquid adhesive force promoted more easily the closely packed assembly of the particles, unlike the strong electrostatic effect of the hydrophilic surface. In order to study the influence of different interface on dimensional changes over time during drying, we measured the change of drop height and contact-line diameter with time. The dot lines in Fig. 2b shows the changing tendency of droplet diameter on hydrophilic and hydrophobic surface, respectively. The diameter of both droplets changed little at the first stage, then both of them dropped quickly at the second stage. The triangulation point line shows the changing tendency of droplet height on hydrophilic and hydrophobic surface (Fig. 2d), both of them decreases linearly. No matter on what type of interface, the droplet diameter and height have same changing tendency.

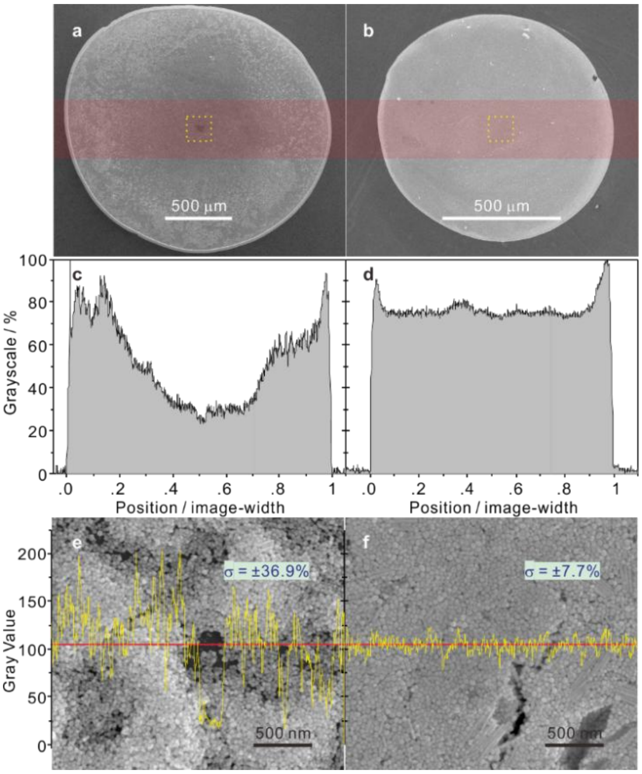

Figure 3. (a and b) Optical images of the deposition area of 1 μl Ag sols on hydrophobic and hydrophilic surfaces, respectively. (c and d) The height profiles plotted by the grayscale values integrated over 20% of the deposition area as highlighted by red colour in a and b, respectively. Noted that the profiles show the inverted grayscale of the photographs, which is a useful relative measure of the deposition distribution but is not an absolute measure of the particle density. (e and f) The corresponding SEM observations on the centre region of the deposition area on hydrophobic and hydrophilic surfaces. The height profiles and the standard deviations (σ) are shown on the corresponding images.

When the droplets placed on each surface dried completely, the interface effects on depostion morphology of nanoparticles were compared between hydrophobic and hydrophilic surfaces (Fig. 3). The SEM images of low magnification illustrated that the final deposition film of a colloidal droplet dried on hydrophilic surface was typically a ring-like structure (Fig. 3a) while this phenomenon was greatly weakened on hydrophobic surface (Fig. 3b). The margin of the ring formed on hydrophilic surface was wide while that on hydrophobic surface was very narrow. Both the initial drop volumes were 1μl, both of the deposited films have an average thickness of larger than 1 μm, the resulting deposition area was 1.9 mm in diameter on hydrophilic surface but 0.8 mm on hydrophobic surface. The surface coverage by particle deposition induced a significant gray difference with silicon surface and hence the film thickness was profiled (Figs. 3c and 3d) by the grayscale analysis of integrating 20% of deposition area as indicated by red belt in Figs. 3a and 3b. Note that the profile shows the gray scale of the photographs, which is a useful relative measure of the deposition distribution in each picture but is not an absolute measure of the particle density. The deposition profiles on hydrophilic surface further illustrated that there are less nanoparticles in the center and most of the particles are deposited on the edge. On hydrophobic surface, particles evenly deposited with only a slightly thick edge. The slightly thick edge is formed owning to much higher evaporation flux at the edge of the droplet.

Coffee ring stains would form when the evaporation rate at the solid/liquid/air triple-phase boundary of the droplet is larger than other region of liquid surfaces, which induces a fluid flux toward the contact line to compensate for solvent loss. As a consequence, suspended particles are dragged toward the contact line where they become deposited.[27] During the drying process, the droplet contact line remains pinned in all suspensions, and fluid (carrying particles) flows outward from the drop center to replenish the edges. Spherical particles are efficiently transported to the edge, either in the bulk or along the air–water interface, leaving a ring after evaporation is complete the same composition.[28] The situation where a capillary force (F) acts on a spherical particle is located at the air−water−substrate. It is convenient to decompose the capillary force into lateral and vertical components: $F_l = F\sin(\theta)$ and $F_v = F\cos(\theta)$, respectively. F_l is responsible for pushing the colloid toward the bulk of the liquid, and F_v is responsible for pinning the particle on the substrate surface. Additionally, a friction force (F_f) is involved to counter balance F_l and represents a resistance for colloids being pushed into the bulk.[29] When $F_f < F_l$,colloids would slip with the receding contact line because friction between the particle and substrate is insufficient to overcome the lateral capillary force acting on the colloid.[30] Colloids on hydrophobic silicon slides slip with the contracting contact line, and would therefore be required to experience an impossible friction against the substrate to remain pinned. The evaporation flux at the edge of the droplet is much higher than that at the center, leading to more solvent loss at the edge of the droplet than at the center. To keep the contact line pinned, the solvent must flow from the droplet center toward the edge to compensate for the solvent loss. Consequently, a flow is generated in the evaporating droplet, then more particles are carried to the edge .[31] The closely-packed assembly of the particles resulted mainly from the liquid adhesive force. Colloids on hydrophobic silicon slides slip with the contracting contact line, which will induce a much larger concentrating effects of the nanoparticles.

Nevertheless, the fluorosilylated surface greatly weakens this effect compared to the hydroxylated one. The SEM observations of high magnification further demonstrated that the roughness (σ, as indicated in Figs. 3e and 3f) of deposited films is about ±36.9% and ±7.7% on the hydrophilic and hydrophobic surfaces, respectively. The electrostatic interaction of the hydroxylated surface should disturb the electric double-layer (Scheme 1f) and induced the electrostatic adsorption of nanoparticles, which certainly contributed to the increase of film roughness. In contrast, our previous study have already reveal that no particles was adsorbed on the hydrophobic surface in the first 9 min.[17] Hence, the closely-packed assembly of the particles resulted mainly from the liquid adhesive force. The fluorosilylated surface produced a rather smaller deposition area (Fig. 3a and b), a more uniform deposition (Fig. 3c and d), and a much smaller roughness (Fig. 3e and f), which significantly differed from the strong electrostatic effect of the hydrophilic surface. These factors certainly induced significant differences in SERS enhancement of 3D hotspot architectures.

3D organization of Ag particles in 3D space

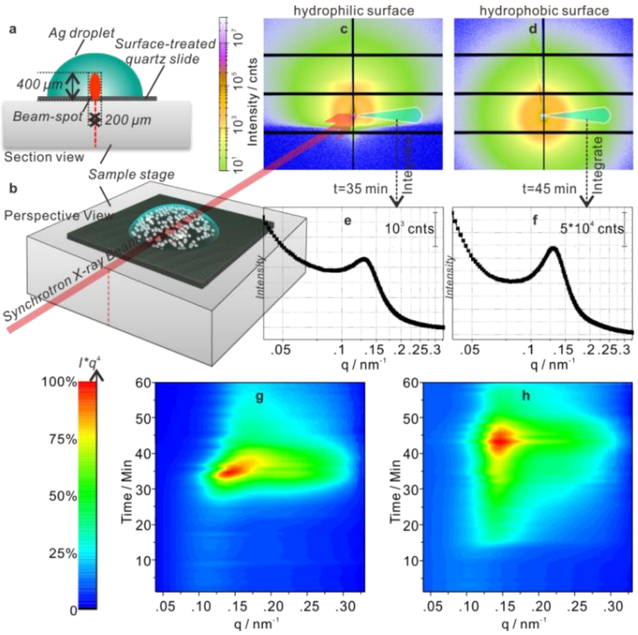

Figure 4. Schematic (a) cross-sectional and (b) perspective views of the experimental setup used for SR-SAXS analysis of a single droplet of a 15 μL Ag sample during the evaporation process, indicating the sample position, the beam-spot size, and the direction of X-ray beam (λ = 1.04 Å). (c and d) Typical 2D SR-SAXS patterns recorded at the specific times with maximal intensities on hydrophilic and hydrophobic surfaces, respectively. (e and f) Their corresponding SR-SAXS curves obtained by integration over an azimuthal range of −165 to 165°, plotted as SR-SAXS intensity (I) vs scattering vector modulus (q). (g and h) Their corresponding time-dependence of the transformed SR-SAXS curves plotted as q^4 Ɨ vs q.

To in situ examine the solid/liquid interface effects on 3D geometry of Ag particles in a droplet during its evaporation process, in situ SR-SAXS was employed to directly monitor a single droplet of concentrated Ag sols placed on the hydroxylated and fluorosilylated quartz slides, respectively, without further sample manipulation. The developed SR-SAXS setup is schematically depicted in Figs. 4a and 4b. Initially, the specific quartz slide was placed on the horizontal sample stage. The X-ray beam with a spot of about 200 μm × 400 μm swept past the surface of the sample slide, and the tilt angle of the sample stage was zero degrees, which ensures the collection of the structural information near the slide surface. In situ SR-SAXS observation with a time resolution of 8 s was performed on a single droplet of 15-μl Ag sols placed in the light path. The evaporation process had a duration of about 1 h. Figs. 4c and 4d present the typical 2D SR-SAXS patterns at specific times by the use of hydrophilic and hydrophobic surfaces, respectively, and the 2D patterns were processed and converted into diagrams of scattered intensities (*I*) vs. scattering vector (*q*) by integration over an azimuthal range of -165~165 ° (Figs. 4e and 4f). The *q* is defined in terms of the scattering angle θ and the radiation wavelength λ as follows: $q=4\pi\sin\theta/\lambda$.

The electron density contrast between the nanoparticles and the solvent or air initiated the scattering signal. The statistical average distance between particles defines the interparticle distance in the 3D geometry of a SAXS sample. In a dense system, the sharp increase in uniformity of interparticle distance will produce a scattering maximum in the scattering curves. Fig. 4e displays the maximal peak at q=0.14 collected on hydrophilic surface. This data implies that the assembly of Ag particles in the evaporation process has a long-range-ordered structure after ~35 min, similarly the maximal peak collected on hydrophobic surface arose after about 45 min. Theoretically, the decrease in the uniformity of the interparticle distance will lower and broaden the scattering maximum; sometimes, the scattering maximum degrades into a shoulder peak, indicating the superposition of interparticle distances of different magnitudes in the scattering curve. The latter phenomenon is more common in both the initial and final stages of the evaporation process. In these cases, the Lorentz correction method was used to accurately determine the position of the scattering maximum; the intensity *I* of the SAXS curves was transformed into q^4*I plotted as a function of q (Figs. 4g and 4h). Figs. 4g and 4h present 2D time-course mapping of q^4*I vs q on two different surfaces, plotted by the total SR-SAXS scattering curves obtained throughout the entire evaporation process. Both of the maximal peaks (q_{max}) clearly indicates the emergence and rightward shift of the signal peak, and it reflects the scattering interference between particles when the interparticle gap (g) decreases to nanometer levels. The interparticle centre-to-centre distance (a) can be estimated by the formula: $a=2\pi/q_{max}$, and then the interparticle gap (g) can be calculated by $g=a-d$, where d is the particle diameter.

It should be noted that there was at least a ten-fold of magnitude difference between the maximum intensity in Fig. 4e and f. The intensities of $q^4 \cdot I$ in Fig. 4g and h were normalized in order to show the variation trend of each spectra set. The long-range-ordered structure of nanoparticles in evaporating sols arose much earlier and last longer on hydrophobic surface (Figs. 4g and 4h). An additional indicator of interparticle distance is the FWHM of the transformed scattering maximum. The rapid right-shift of the red-color area in Fig. 4g indicated a faster broadening of the SAXS peaks. More regular interparticle distances will produce higher and narrower peaks. Considering these two aspects, hydrophobic surface creates a more regular long-range structure which resulted in a smaller FWHM and a higher and narrower peak on each SR-SAXS curve. To deep insight into the 3D organization of particles on each surface, we hypothesized that each curve of q^4*I plotted as a function of q is the ensemble reflection of three existential states of particles in a droplet: State I, free individual particles with $g >> 1$ nm corresponding to a values of larger than d; State II, 3D hotspot geometry of particles trapped in trapping well with g ≈ 2-3 nm corresponding to a values of close to d; and State III, particle aggregation with $g = 0$ corresponding to $a \le d$.

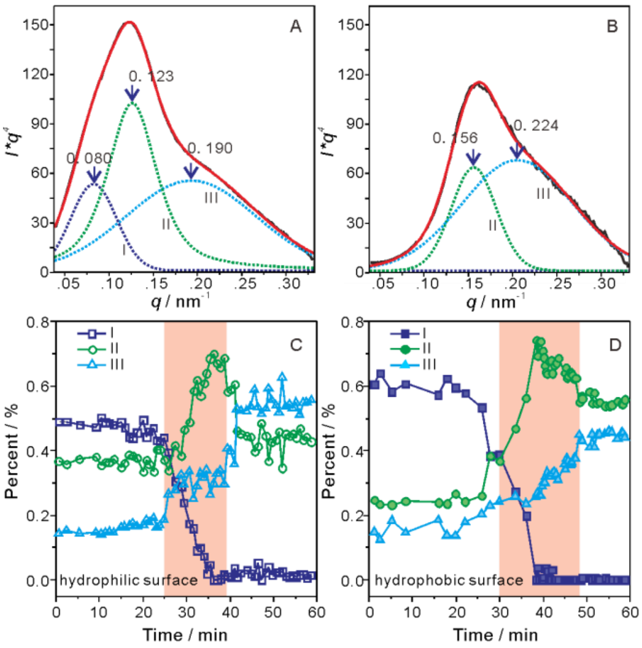

Figure 5. (A, B) The normalized SR-SAXS curves (black solid-lines) recorded on hydrophobic surface at 40 min and 50 min, respectively, and their corresponding Gaussian fitting (red solid-lines) deconvoluted into three basis curves (blue, green, and cyan dot-lines). (C and D) The fraction of each basis curve contributing to each experimental curve at different times on hydrophilic and hydrophobic surfaces, respectively. The fractional weights of the three basis curves were considered to be representative of free individual particles (State I), 3D geometry of particles trapped in trapping well (State II), and particle aggregation (State III).

Mathematically, each state could be reflected by a Gaussian fitting curve featured by q^4*I maximum at a specific q value (q_{max}). Figs. 5a and 5b illustrated that each curve collected both on hydrophilic and hydrophobic surfaces could be well fitted by Gaussian curves with three q values: 0.08 nm^{-1}, 0.12 nm^{-1}, and 0.19 nm^{-1}. These three q values correspond to g values of 28.5 nm, 2.3 nm, and -17.0 nm, respectively. The calculated negative value of g implies the solid aggregating and stacking of particles on the slide surface. On the basis of curve fitting, each component proportion of those three kinds of particles was estimated (Figs. 5c and 5d). In the early stages, the hydrophobic surface makes more free particles (State I in Fig. 5) than hydrophilic surface. That is to say, the nanoparticles have a stronger tendency to aggregate on hydrophilic surfaces. In the enhancing stages, the number of trapped particles (State II in Fig. 5) sharply increased on both two kinds of surfaces. This kind of increase is a temporary phenomenon, but the number of trapped particles on hydrophobic surface maintains at a higher level and lasts a longer time than hydrophilic one. In the final stages of evaporation process, the number of trapped particles on hydrophilic surface sharply decreased to the level similar with the initial state but that on hydrophobic surface maintains at a higher level compared with the initial state, which is consistent with more orderly arrangement of nanoparticles on hydrophobic surface (Figs. 2e and 2f). These diffrences should be responsible for the huge differences in SERS properties. In brief, this kind of pure mathematical transforming did not correspond to strict physical image and might be biased to characterize the particle ensemble, however, it could reveal, to a certain extent, the intrinsic mechanism of hydrophobic surface-enhanced regulation of particle deposition.

Robust SERS identification of chemicals remains an attractive challenge because of the inefficient use of hotspots in 1D and 2D geometries of SERS hotspots. Hence, it is particularly valuable to constructing 3D hotspots in space. But only very few examples of well-defined 3D geometry of SERS hotspots have been reported. Our experimental evidence derived from in situ SR-SAXS reveals that a truly distinct 3D geometry of the Ag particles develops during the evaporation process on both hydrophilic and hydrophobic surfaces (Scheme 1b). This type of 3D geometry significantly differs from the particle assembly in dry state and has a maximal uniformity of interparticle distance. Particularly, the fluorosilylated surface reduces the interaction with particles and decreases the ability of electrostatic adsorption, which helps to control the interparticle distance in a small range. The modified surface properties certainly produce a larger number of hot spots in 3D space and accordingly amplify the SERS enhancement (Scheme 1c). And in closing, it is worth speculating on the origin of the difference in SERS performances of two kinds of flat surface. The presence of electrostatic hydroxyl groups on hydrophilic surface could interact with the potential ions in electric double-layer of each colloidal particle, consequently disturb or even destroy the electric double-layer (Scheme 1f), and finally induce the electrostatic adsorption of nanoparticles. With regard to the electrostatic adsorption, the hydrophobic surface not only can serve as a concentrator of nanoparticles for increased SERS signals, but also has the ability to concentrate dissolved analytes in dilute aqueous solutions. Such a driving force caused by hydrophobicity is very beneficial for molecules to get trapped in the hot-spot areas.[24, 32] Hence, the hydrophobic surface increases the synergistic effect of nanoparticle behaviors and then increases the existing possibility of 3D hotspot and targeting analytes in laser irradiation volume, which greatly enhanced the SERS signals compared to the hydrophilic surface and the dried states of nanoparticles. This will shed some light on controlling 3D geometry of SERS hotspots that extends in all three dimensions.

Conclusions

This study highlights the differences of hydrophilic and hydrophobic surfaces in enhanced Raman scattering by the use of extremely diluted R6G molecules as the SERS reporter. In situ SR-SAXS technique provides insights into the evolution of the 3D geometry of Ag nanoparticles in a single droplet and verify the influence mechanism of this two kinds of surfaces. A progressive 3D self-assembly of nanoparticles was more preferred due to the interface effects, however, 3D hotspots would always appear in the evaporating sols at a specific moment because of the liquid adhesive force promotes the closely packed assembly of the particles in 3D space, although the present work demonstrates that the hydrophobic surface has a greater potential as a SERS effective supporting substrate and it could be expected that hydrophobic surface can be practically used for the rapid trace analysis in the near future. Nevertheless, how to control the lasting time of 3D hotspots and increasing its life is affected by many environmental factors, and the answer to utilize the capillary force to stably and reproducibly construct 3D geometry of nanoparticles in space is an important research direction in the future.

Acknowledgements

This work was supported by the National Basic Research Program of China (2011CB933700), the National Instrumentation Program of China (2011YQ0301241001 & 2011YQ0301241101), CETC Technological Innovation Fund (JJ-QN-2013-35), National Natural Science Foundation of China (21305142), and Natural Science Foundation of Anhui Province, China (1308085QB27).

Notes and references

[a] *Institute of Intelligent Machines, Chinese Academy of Sciences, Hefei 230031 (China). Fax: (+86)551-65592420, E-mail: hlliu@iim.ac.cn , lbyang@iim.ac.cn*
[b] *No.38 Research Institute of China Electronics, Technology Group Corporation, Hefei 230088 (P.R. China).*

† Electronic Supplementary Information (ESI) available: Calculation of the focal volume, Effects of focal depth. See DOI: 10.1039/b000000x/

‡ These authors contributed equally to this work.

1. S. Schlücker, *Angew. Chem. Int. Edit.*, 2014, **53**, 2-42.
2. H. K. Lee, Y. H. Lee, I. Y. Phang, J. Wei, Y.-E. Miao, T. Liu and X. Y. Ling, *Angew. Chem. Int. Edit.*, 2014, 5154-5158.
3. H. Liu, Y. Sun, Z. Jin, L. Yang and J. Liu, *Chem. Sci.*, 2013, **4**, 3490-3496.
4. J.-H. Lee, J.-M. Nam, K.-S. Jeon, D.-K. Lim, H. Kim, S. Kwon, H. Lee and Y. D. Suh, *ACS Nano*, 2012, **6**, 9574-9584.
5. H. Liu, D. Lin, Y. Sun, L. Yang and J. Liu, *Chem-Eur J.*, 2013, **19**, 8789-8796.
6. S. J. Barrow, A. M. Funston, D. E. Gómez, T. J. Davis and P. Mulvaney, *Nano Lett.*, 2011, **11**, 4180-4187.
7. J. A. Fan, C. Wu, K. Bao, J. Bao, R. Bardhan, N. J. Halas, V. N. Manoharan, P. Nordlander, G. Shvets and F. Capasso, *Science*, 2010, **328**, 1135-1138.
8. M. P. Cecchini, V. A. Turek, J. Paget, A. A. Kornyshev and J. B. Edel, *Nat. Mater.*, 2013, **12**, 165-171.
9. K. Jung, J. Hahn, S. In, Y. Bae, H. Lee, P. V. Pikhitsa, K. Ahn, K. Ha, J.-K. Lee, N. Park and M. Choi, *Adv. Mater.*, 2014, **26**, 5924-5929.
10. M. Chirumamilla, A. Toma, A. Gopalakrishnan, G. Das, R. P. Zaccaria, R. Krahne, E. Rondanina, M. Leoncini, C. Liberale, F. De Angelis and E. Di Fabrizio, *Adv. Mater.*, 2014, **26**, 2353-2358.
11. P. Goldberg-Oppenheimer, S. Mahajan and U. Steiner, *Adv. Mater.*, 2012, **24**, Op175-Op180.
12. H. Ko, S. Chang and V. V. Tsukruk, *ACS Nano*, 2009, **3**, 181-188.
13. H. Ko and V. V. Tsukruk, *Small*, 2008, **4**, 1980-1984.
14. Q. Zhang, Y. H. Lee, I. Y. Phang, C. K. Lee and X. Y. Ling, *Small*, 2014, **10**: 2703-2711.
15. M. S. Chen, I. Y. Phang, M. R. Lee, J. K. W. Yang and X. Y. Ling, *Langmuir*, 2013, **29**, 7061-7069.
16. N. Pazos-Perez, C. S. Wagner, J. M. Romo-Herrera, L. M. Liz-Marzan, F. J. G. de Abajo, A. Wittemann, A. Fery and R. A. Alvarez-Puebla, *Angew. Chem. Int. Edit.*, 2012, **51**, 12688-12693.
17. H. Liu, Z. Yang, L. Meng, Y. Sun, J. Wang, L. Yang, J. Liu and Z. Tian, *J. Am. Chem. Soc.*, 2014, **136**, 5332-5341.

18. L. Yang, H. Liu, J. Wang, F. Zhou, Z. Tian and J. Liu, *Chem. Commun.*, 2011, **47**, 3583-3585.
19. H. Zhou, Z. Zhang, C. Jiang, G. Guan, K. Zhang, Q. Mei, R. Liu and S. Wang, *Anal. Chem.*, 2011, **83**, 6913-6917.
20. L. Yang, H. Liu, Y. Ma and J. Liu, *Analyst*, 2012, **137**, 1547-1549.
21. K. Kim, H. S. Han, I. Choi, C. Lee, S. Hong, S.-H. Suh, L. P. Lee and T. Kang, *Nat. Commun.*, 2013, **4**.
22. J. Ilavsky and P. R. Jemian, *J. Appl. Crystallogr.*, 2009, **42**, 347-353.
23. E. C. Le Ru and P. G. Etchegoin, in *Principles of Surface-Enhanced Raman Spectroscopy*, eds. E. C. L. Ru and P. G. Etchegoin, Elsevier, Amsterdam, 2009, pp. 1-27.
24. L.-Q. Lu, Y. Zheng, W.-G. Qu, A.-W. Xu and H.-Q. Yu, *J. Mater. Chem.*, 2012, **22**, 20986.
25. P. J. Yunker, T. Still, M. A. Lohr and A. G. Yodh, *Nature*, 2011, **476**, 308-311.
26. K. Han, Z. Zhang, S. T. Wereley and J. H. Oh, Study of Factors in Coffee-Ring Structure Formation Using PIV Methods, 2011, 1069-1075.
27. H. Hu and R. G. Larson, *J. Phys. Chem. B*, 2002, **106**, 1334-1344.
28. P. J. Yunker, T. Still, M. A. Lohr and A. G. Yodh, *Nature*, 2011, **476**, 308-311.
29. B. Gao, T. S. Steenhuis, Y. Zevi, V. L. Morales, J. L. Nieber, B. K. Richards, J. F. McCarthy and J.-Y. Parlange, *Water Resources Research*, 2008, **44**, W04504.
30. V. L. Morales, J.-Y. Parlange, M. Wu, F. J. Perez-Reche, W. Zhang, W. Sang and T. S. Steenhuis, *Langmuir*, 2013, **29**, 1831–1840.
31. H. Hu and R. G. Larson, *Langmuir*, 2005, **21**, 3963-3971.
32. K. Qian, L. Yang, Z. Li and J. Liu, *J. Raman Spectrosc.*, 2013, **44**, 21-28.